

ARTICLE OPEN

A thermodynamic potential for barium zirconate titanate solid solutions

Jinlin Peng¹, Dongliang Shan¹, Yunya Liu¹, Kai Pan¹, Chihou Lei², Ningbo He¹, Zhenyu Zhang¹ and Qiong Yang¹

Barium zirconate titanate [Ba(Zr_xTi_{1-x})O₃] solid solutions are promising lead-free ferroelectric materials that have received substantial interest. Thermodynamic analysis based on phenomenological Landau–Devonshire theory is a powerful method for theoretical investigation of ferroelectric materials, but cannot be applied to Ba(Zr_xTi_{1-x})O₃ because there is no thermodynamic potential. In this paper, a thermodynamic potential for Ba(Zr_xTi_{1-x})O₃ (0 ≤ x ≤ 0.3) solid solutions is constructed, and then a thermodynamic analysis carried out. The results accurately reproduce known phase structures and their transition temperatures, with good agreement with experimentally measured polarization, dielectric, and piezoelectric constants. It is found that Ba(Zr_xTi_{1-x})O₃ solid solutions at room temperature have three phase boundaries, including a tetragonal–orthorhombic phase boundary at x = 0.013, an orthorhombic–rhombohedral phase boundary at x = 0.0798, and a rhombohedral–paraelectric phase boundary at x = 0.2135. The results also indicate that the chemical composition-induced ferroelectric–paraelectric phase boundary has superior electromechanical properties, suggesting a new way to enhance electromechanical coupling in Ba(Zr_xTi_{1-x})O₃ solid solutions.

npj Computational Materials (2018)4:66; doi:10.1038/s41524-018-0126-3

INTRODUCTION

Ferroelectrics with switchable polarization, excellent dielectric, piezoelectric, and pyroelectric properties have a wide range of applications in memories, capacitors, actuators, sensors, and electrocaloric cooling devices.^{1–12} As a typical ferroelectric material, barium titanate (BaTiO₃) possesses a rich variety of phase transitions.¹³ Above its Curie temperature ($T_C \sim 120^\circ\text{C}$), the BaTiO₃ single crystal is paraelectric phase with cubic symmetry.¹³ When the BaTiO₃ single crystal is cooled through Curie temperature, it undergoes a paraelectric to ferroelectric phase transition, and has a tetragonal phase structure with polarization along <100> direction.¹³ When the cooling is continued, the BaTiO₃ single crystal exhibits a tetragonal ferroelectric to orthorhombic ferroelectric phase transition at about $T_{T \leftrightarrow O} \sim 0^\circ\text{C}$ with polarization along <110> direction.¹³ Upon further cooling, the BaTiO₃ single crystal shows an orthorhombic ferroelectric to rhombohedral ferroelectric phase transition around $T_{O \leftrightarrow R} \sim -80^\circ\text{C}$ with polarization along <111> direction.¹³ Thus, BaTiO₃ has three types of phase transitions, including one ferroelectric–paraelectric (FE–PE) phase transition and two ferroelectric–ferroelectric (FE–FE) phase transitions. The corresponding phase transition temperatures can be tuned by the substitution of Ti⁴⁺ with Zr⁴⁺,^{14,15} which forms barium zirconate titanate [Ba(Zr_xTi_{1-x})O₃] solid solutions. In Ba(Zr_xTi_{1-x})O₃ system, the FE–FE phase transition temperatures $T_{T \leftrightarrow O}$ and $T_{O \leftrightarrow R}$ increase with the increase in composition of Zr, whereas the FE–PE phase transition temperature T_C decreases with increasing composition x, and all three phase transitions are pinched into a single phase transition around x = 0.15,^{15,16} suggesting a pinched phase transition feature. With further increase in composition x, Ba(Zr_xTi_{1-x})O₃ solid solutions only have FE–PE phase transitions between rhombohedral and cubic phase

structures, and the corresponding phase transition temperature T_C decreases.¹⁵

Ba(Zr_xTi_{1-x})O₃ solid solutions have been studied widely on the experimental aspects. For example, the phase structures of Ba(Zr_xTi_{1-x})O₃ solid solutions at different temperatures were investigated by Yu^{16,17} et al., and the phase transition temperatures were identified for the low-composition range (x = 0, 0.05, 0.08, 0.1, 0.15, 0.2, 0.25, 0.3),^{13,16–22} revealing that a pinched phase transition occurs near the composition x = 0.15.^{15,16} Also, previous experimental observations displayed that Ba(Zr_xTi_{1-x})O₃ with composition x = 0.08 has a coexistence of orthorhombic and rhombohedral phases at a temperature of 30 °C, and possesses an enhancement of piezoelectric response near this polymorphic phase boundary.²² In addition, Yu et al. studied the dielectric properties of Ba(Zr_xTi_{1-x})O₃ solid solutions, and found that Ba(Zr_xTi_{1-x})O₃ solid solutions have stronger dielectric response than that of pure BaTiO₃.²¹ Recently, Qian et al. discovered that Ba(Zr_xTi_{1-x})O₃ solid solutions show a giant electrocaloric effect over a broad temperature range.²³ Thus, the previous experimental results indicate that Ba(Zr_xTi_{1-x})O₃ solid solutions have great potential applications. However, the phase diagram and electromechanical properties with continuous variation in composition have not been accomplished.

Although the experimental advances in Ba(Zr_xTi_{1-x})O₃ solid solutions are encouraging, the corresponding theoretical studies are rare. Thermodynamic analysis based on phenomenological Landau–Devonshire theory is a powerful method for the theoretical investigation of ferroelectric materials.^{3,7,24–35} In order to implement thermodynamic analysis, the thermodynamic potential of a particular ferroelectric system should be established first. Haun et al. have established the thermodynamic potential for lead zirconate titanate (PZT) solid solution based on its phase

¹Key Laboratory of Low Dimensional Materials and Application Technology of Ministry of Education, School of Materials Science and Engineering, Xiangtan University, Hunan 411105, China and ²Department of Aerospace and Mechanical Engineering, Saint Louis University, Saint Louis, MO 63103, USA
Correspondence: Yunya Liu (ylyiu@xtu.edu.cn)

Received: 30 March 2018 Accepted: 13 November 2018

Published online: 30 November 2018

structures and electromechanical properties in single crystals and bulk ceramics.³⁶ Similarly, Bell and Cross³⁷ constructed a sixth-order thermodynamic potential for BaTiO₃, which was revised as an eighth-order thermodynamic potential by Li et al.²⁶ After that, Wang et al.³⁸ reported another eighth-order thermodynamic potential, in which the second and higher-order coefficients are dependent on temperature. In order to consider the quantum mechanical effects at low temperature, Wang et al.³⁹ proposed a modified thermodynamic potential for BaTiO₃, based on which the calculated phase transitions in temperature–pressure phase diagram show excellent agreement with experimental data. With the established thermodynamic potentials, the thermodynamic analysis on PZT solid solution and BaTiO₃ have been implemented widely for explaining and predicting new physical phenomena.^{40–42} On the other hand, the known thermodynamic potential is a necessary condition for simulating ferroelectric domain structures via the conventional phase-field method.^{43–46} Thus, thermodynamic potential plays an important role in the theoretical analysis of ferroelectrics. However, the thermodynamic potential of Ba(Zr_xTi_{1–x})O₃ solid solutions is unestablished and lacking. This is also one reason for rare theoretical studies on Ba(Zr_xTi_{1–x})O₃ solid solutions. Thus, we seek to construct thermodynamic potential for Ba(Zr_xTi_{1–x})O₃ (0 ≤ x ≤ 0.3) solid solutions, and then employ it to study and predict the phase diagram as well as electromechanical properties of Ba(Zr_xTi_{1–x})O₃ solid solutions via theoretical analysis.

RESULTS AND DISCUSSION

Constructing thermodynamic potential

Thermodynamic potential is the key factor for the thermodynamic theory of ferroelectrics, which is lacking for Ba(Zr_xTi_{1–x})O₃ solid solutions. Thus, we seek to construct it for Ba(Zr_xTi_{1–x})O₃ solid solutions. Based on the phenomenological Landau–Devonshire theory, the thermodynamic potential always uses polarization as an order parameter to describe the phase transitions in ferroelectrics.³⁶ With the free energy of paraelectric phase at Curie

temperature as a reference, the thermodynamic potential energy of a ferroelectric crystal under isothermal condition can be expanded in powers of polarization P_i ($i = 1, 2, 3$) and stress σ_j ($j = 1, 2, \dots, 6$),^{47–49}

$$G = \alpha_1(P_1^2 + P_2^2 + P_3^2) + \alpha_{11}(P_1^4 + P_2^4 + P_3^4) + \alpha_{12}(P_1^2P_2^2 + P_1^2P_3^2 + P_2^2P_3^2) + \alpha_{111}(P_1^6 + P_2^6 + P_3^6) + \alpha_{112}[P_1^4(P_2^2 + P_3^2) + P_2^4(P_1^2 + P_3^2) + P_3^4(P_1^2 + P_2^2)] + \alpha_{123}P_1^2P_2^2P_3^2 + \alpha_{1111}(P_1^8 + P_2^8 + P_3^8) + \alpha_{1122}(P_1^4P_2^4 + P_1^4P_3^4 + P_2^4P_3^4) + \alpha_{1112}[P_1^2(P_2^6 + P_3^6) + P_2^2(P_1^6 + P_3^6) + P_3^2(P_1^6 + P_2^6)] + \alpha_{1123}(P_1^2P_2^4P_3^4 + P_1^4P_2^2P_3^4 + P_1^4P_2^4P_3^2) - \frac{5\mu}{2}(\sigma_1^2 + \sigma_2^2 + \sigma_3^2) - \frac{5\nu}{2}(\sigma_4^2 + \sigma_5^2 + \sigma_6^2) - S_{12}(\sigma_1\sigma_2 + \sigma_2\sigma_3 + \sigma_1\sigma_3) - Q_{11}(\sigma_1P_1^2 + \sigma_2P_2^2 + \sigma_3P_3^2) - Q_{12}[\sigma_3(P_1^2 + P_2^2) + \sigma_2(P_1^2 + P_3^2) + \sigma_1(P_2^2 + P_3^2)] - Q_{44}(\sigma_6P_1P_2 + \sigma_4P_2P_3 + \sigma_5P_1P_3) - P_1E_1 - P_2E_2 - P_3E_3, \quad (1)$$

in which E_i is the electric field, Q_{ij} , S_{ij} are the electrostrictive coefficient and elastic compliance constant under constant polarization in Voigt notation, respectively. It should be noted that α_1 , α_{ij} , α_{ijk} , and α_{ijkl} are the thermodynamic potential coefficients, all of which are unknown for Ba(Zr_xTi_{1–x})O₃ solid solutions. Estimating the values of these coefficients can then construct the thermodynamic potential of Ba(Zr_xTi_{1–x})O₃ solid solutions.

According to the thermodynamic theory, phase structures and electromechanical properties of ferroelectrics can be calculated using thermodynamic analysis from thermodynamic potential.^{36,49} The polarization of ferroelectrics can be determined by minimizing thermodynamic potential, that is, by solving the derivatives of thermodynamic potential with respect to polarization components for zeros,

$$\frac{\partial G}{\partial P_1} = 0, \frac{\partial G}{\partial P_2} = 0, \frac{\partial G}{\partial P_3} = 0. \quad (2)$$

The phase structures are classified by the solutions of the equilibrium polarization states, which include four sets of solutions corresponding to four different phase structures: (i) the paraelectric (PE) phase with $P_1 = P_2 = P_3 = 0$; (ii) the tetragonal (T) phase with P_1

Table 1. Coefficients of thermodynamic potential, elastic compliance constants, and electrostrictive coefficients of Ba(Zr_xTi_{1–x})O₃ solid solutions

Coefficient	Composition x in Ba(Zr _x Ti _{1–x})O ₃							
	0 ^a	0.05	0.08 ^b	0.1	0.15	0.2	0.25	0.3
T_0 (°C)	115	107	100	84	64	32	–10	–52
α_1 ^c [$10^5 \text{m}^2 \text{N}/(\text{C}^2 \cdot ^\circ \text{C})$]	4.124	4.6	4.45	3.53	3.45	3.12	1.9	1.6
α_{11} ($10^8 \text{m}^6 \text{N}/\text{C}^4$)	–2.097	–1.98	–1.964	–1.5	–4.66	–15.1	–17.2	–19.2
α_{12} ($10^8 \text{m}^6 \text{N}/\text{C}^4$)	7.974	12.54	12.66	7.22	0.87	0.12	0.06	0.03
α_{111} ($10^9 \text{m}^{10} \text{N}/\text{C}^6$)	1.294	5.8	9.986	15.2	79	370	778	1153
α_{112} ($10^9 \text{m}^{10} \text{N}/\text{C}^6$)	–1.95	–9.85	–19.42	–18.5	–13.28	–5.28	–2.88	–2.38
α_{123} ($10^9 \text{m}^{10} \text{N}/\text{C}^6$)	–2.5	–5.72	–2.132	–1.8	–1.2	–0.75	–0.35	–0.15
α_{1111} ($10^{10} \text{m}^{14} \text{N}/\text{C}^8$)	3.863	9.65	15.08	14.3	9.1	0	0	0
α_{1112} ($10^{10} \text{m}^{14} \text{N}/\text{C}^8$)	2.529	4.421	6.333	9.4	12.5	0	0	0
α_{1122} ($10^{10} \text{m}^{14} \text{N}/\text{C}^8$)	1.637	4.821	8.005	10.5	12.6	0	0	0
α_{1123} ($10^{10} \text{m}^{14} \text{N}/\text{C}^8$)	1.367	1.422	11.15	16.2	10.38	0	0	0
S_{11} ($10^{-12} \text{m}^2/\text{N}$)	8.3–4.87x							
S_{12} ($10^{-12} \text{m}^2/\text{N}$)	–2.7 + 2.025x							
S_{44} ($10^{-12} \text{m}^2/\text{N}$)	9.24 + 5.05x							
Q_{11} (m^4/C^2)	0.1–0.004x							
Q_{12} (m^4/C^2)	–0.034–0.005x							
Q_{44} (m^4/C^2)	0.029 + 0.002x							

^aReference 26
^bReference 50
^cNote that $\alpha_1 = \alpha_1^*(T - T_0)$

$= P_2 = 0, P_3 \neq 0$ (or $P_1 = P_3 = 0, P_2 \neq 0; P_2 = P_3 = 0, P_1 \neq 0$), (iii) the orthorhombic (O) phase with $P_1 = 0, |P_2| = |P_3| \neq 0$ (or $P_2 = 0, |P_1| = |P_3| \neq 0; P_3 = 0, |P_1| = |P_2| \neq 0$); and (iv) the rhombohedral (R) phase with $|P_1| = |P_2| = |P_3| \neq 0$. With the determination of polarization, the relative dielectric constants can be evaluated by

$$\varepsilon_{ij} = 1 + \frac{\eta_{ij}}{\varepsilon_0} \quad (3)$$

with ε_0 being the permittivity of free space and

$$\eta = \begin{pmatrix} \frac{\partial^2 G}{\partial P_1 \partial P_1} & \frac{\partial^2 G}{\partial P_1 \partial P_2} & \frac{\partial^2 G}{\partial P_1 \partial P_3} \\ \frac{\partial^2 G}{\partial P_2 \partial P_1} & \frac{\partial^2 G}{\partial P_2 \partial P_2} & \frac{\partial^2 G}{\partial P_2 \partial P_3} \\ \frac{\partial^2 G}{\partial P_3 \partial P_1} & \frac{\partial^2 G}{\partial P_3 \partial P_2} & \frac{\partial^2 G}{\partial P_3 \partial P_3} \end{pmatrix}^{-1} \quad (4)$$

The piezoelectric coefficients d_{in} ($n = 1, 2, \dots, 6$)

$$d_{in} = \frac{\partial \varepsilon_n}{\partial E_i} = \frac{\partial \varepsilon_n}{\partial P_1} \eta_{i1} + \frac{\partial \varepsilon_n}{\partial P_2} \eta_{i2} + \frac{\partial \varepsilon_n}{\partial P_3} \eta_{i3}, \quad (5)$$

where the strain ε_n can be obtained by the relationship

$$\varepsilon_n = -\frac{\partial G}{\partial \sigma_n}. \quad (6)$$

The above derivation of thermodynamic analysis reveals that phase structures and electromechanical properties of ferroelectrics are correlated with thermodynamic potential directly. As such, the inverse determination of thermodynamic potential coefficients of $\text{Ba}(\text{Zr}_x\text{Ti}_{1-x})\text{O}_3$ solid solutions can be estimated via fitting the available experimental data of phase structures, phase transition temperatures, polarization, and dielectric constants reported in literatures.^{13,16–22,26,50–57} The experimental data used for fitting are listed in Supplementary Table S1. The details of determining thermodynamic potential coefficients for $\text{Ba}(\text{Zr}_x\text{Ti}_{1-x})\text{O}_3$ solid solutions are given in section METHODS and schematically illustrated in Supplementary Fig. S1. A similar procedure has been applied successfully to construct the thermodynamic potentials for $(\text{K}_{1-x}\text{Na}_x)\text{NbO}_3$ and $(\text{Ba}_{1-x}\text{Sr}_x)\text{TiO}_3$.^{58,59} The determined thermodynamic potential coefficients of $\text{Ba}(\text{Zr}_x\text{Ti}_{1-x})\text{O}_3$ solid solutions are tabulated in Table 1.

It is noticed that electromechanical coupling terms are also included in the thermodynamic potential energy [Eq. (1)], and can be determined if elastic compliance constant S_{IJ} and electrostrictive coefficient Q_{IJ} are known. Since the elastic compliance constants and electrostrictive coefficients data of $\text{Ba}(\text{Zr}_x\text{Ti}_{1-x})\text{O}_3$ are unavailable in literature, both of them are evaluated from a linear interpolation of the corresponding data of BaTiO_3 and BaZrO_3 , given by $S_{IJ} = (1-x)S_{IJ}^{\text{BaTiO}_3} + xS_{IJ}^{\text{BaZrO}_3}$ and $Q_{IJ} = (1-x)Q_{IJ}^{\text{BaTiO}_3} + xQ_{IJ}^{\text{BaZrO}_3}$. A similar method was adopted by Huang et al. to obtain the electrostrictive coefficients of $(\text{Ba}_{1-x}\text{Sr}_x)\text{TiO}_3$.⁵⁹ Notice that $S_{11}^{\text{BaTiO}_3} = 8.3 \times 10^{-12} \text{m}^2/\text{N}$, $S_{12}^{\text{BaTiO}_3} = -2.7 \times 10^{-12} \text{m}^2/\text{N}$, $S_{44}^{\text{BaTiO}_3} = 9.24 \times 10^{-12} \text{m}^2/\text{N}$, $S_{11}^{\text{BaZrO}_3} = 3.43 \times 10^{-12} \text{m}^2/\text{N}$, $S_{12}^{\text{BaZrO}_3} = -0.675 \times 10^{-12} \text{m}^2/\text{N}$, $S_{44}^{\text{BaZrO}_3} = 14.29 \times 10^{-12} \text{m}^2/\text{N}$, $Q_{11}^{\text{BaTiO}_3} = 0.1 \text{m}^4/\text{C}^2$, $Q_{12}^{\text{BaTiO}_3} = -0.034 \text{m}^4/\text{C}^2$, and $Q_{44}^{\text{BaTiO}_3} = 0.029 \text{m}^4/\text{C}^2$.^{29,60,61} Due to the lack of available data, we adopt the similar method described by Wang et al.,⁶² and obtain the electrostrictive coefficients of BaZrO_3 ($Q_{11}^{\text{BaZrO}_3} = 0.096 \text{m}^4/\text{C}^2$, $Q_{12}^{\text{BaZrO}_3} = -0.039 \text{m}^4/\text{C}^2$, and $Q_{44}^{\text{BaZrO}_3} = 0.031 \text{m}^4/\text{C}^2$) using combined first-principles calculations and Berry's phase approach (details in the Supporting Information). Since experimental data of electrostrictive coefficients of BaZrO_3 are not available, we compare the hydrostatic electrostrictive coefficient $Q_h = Q_{11} + 2Q_{12}$ between the calculation and experiment, and good agreement is observed, as details in the Supporting Information. As such, the thermodynamic potential of $\text{Ba}(\text{Zr}_x\text{Ti}_{1-x})\text{O}_3$ solid solutions has been constructed, as tabulated in Table 1. The known thermodynamic potential allows us to carry out thermodynamic analysis for $\text{Ba}(\text{Zr}_x\text{Ti}_{1-x})\text{O}_3$ solid solutions, and also makes it possible to realize phase-field simulations for $\text{Ba}(\text{Zr}_x\text{Ti}_{1-x})\text{O}_3$ solid solutions. At low temperature, phase transitions and electromechanical properties of ferroelectrics are significantly affected by low-temperature quantum mechanical effects,^{39,63} which is not considered in this work, due to the lack of corresponding low-temperature experimental data of $\text{Ba}(\text{Zr}_x\text{Ti}_{1-x})\text{O}_3$ solid solutions for fitting thermodynamic potential coefficients.

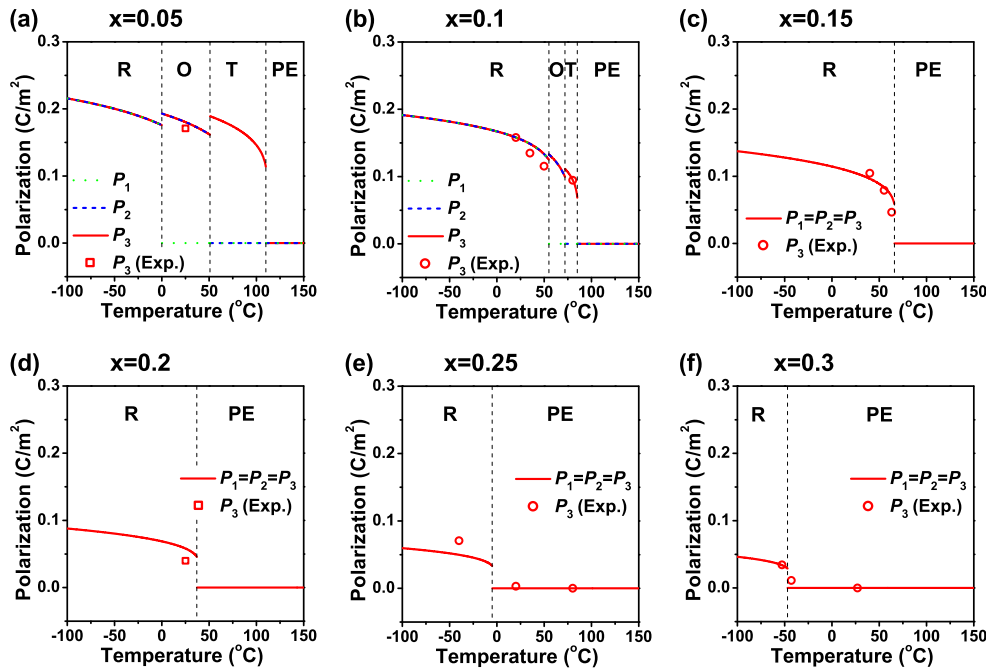


Fig. 1 Polarization of $\text{Ba}(\text{Zr}_x\text{Ti}_{1-x})\text{O}_3$ solid solutions as a function of temperature. **a** $x = 0.05$, **b** $x = 0.1$, **c** $x = 0.15$, **d** $x = 0.2$, **e** $x = 0.25$, and **f** $x = 0.3$, the experimental data of P_3 [**a**,¹⁶, **b**,⁵¹, **c**,⁵², **d**,²⁰, **e**,⁵³, **f**,⁵⁴] denoted by squares (single-crystalline values measured in experiments) and circles (single-crystalline values evaluated⁶⁴ by using ceramic values measured in experiments)

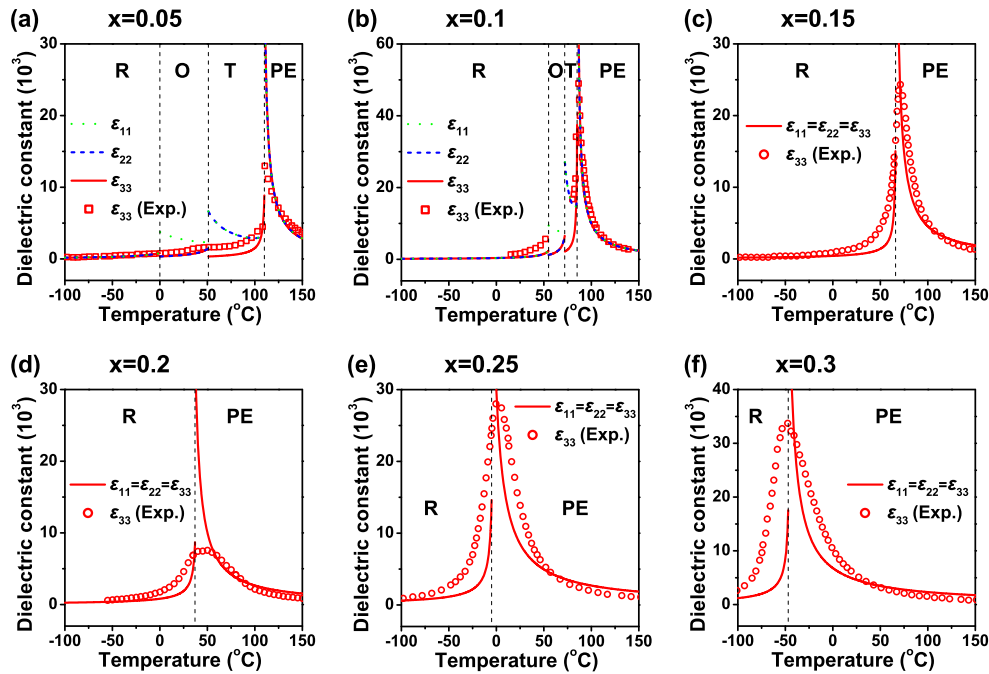


Fig. 2 Dielectric constants of $\text{Ba}(\text{Zr}_x\text{Ti}_{1-x})\text{O}_3$ solid solutions as a function of temperature. **a** $x = 0.05$, **b** $x = 0.1$, **c** $x = 0.15$, **d** $x = 0.2$, **e** $x = 0.25$, and **f** $x = 0.3$, the experimental data of ϵ_{33} [a,⁵⁵ b,¹⁹ c,⁵⁶ d,⁵⁷ e, and f²¹] denoted by squares (single crystals) and circles (ceramics)

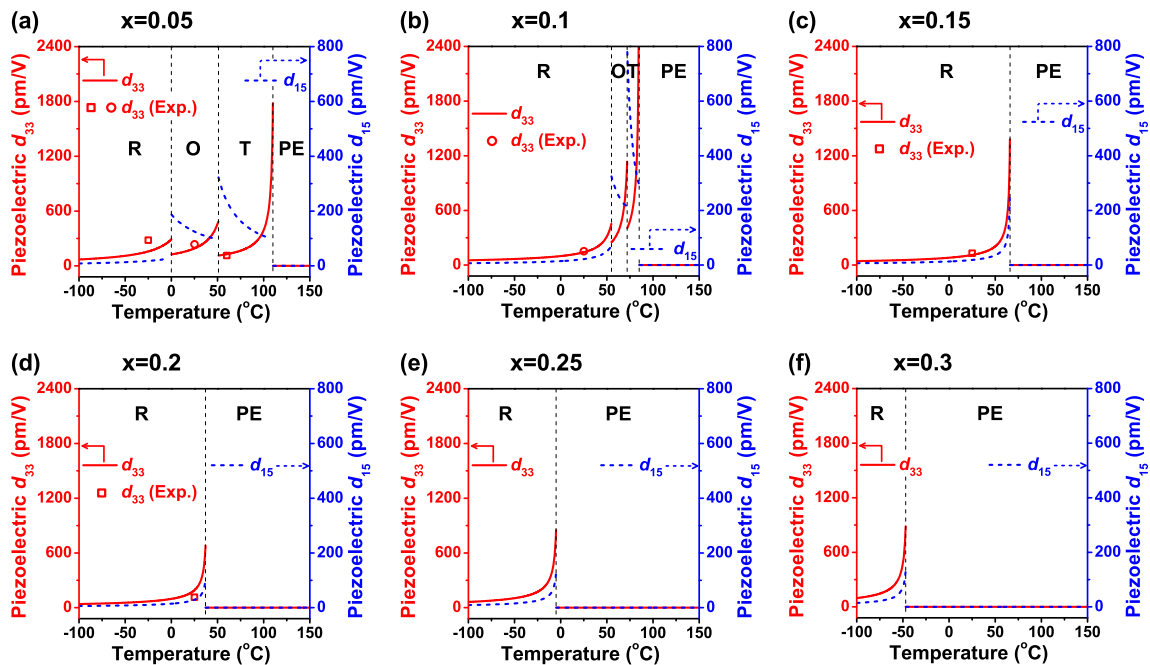


Fig. 3 Piezoelectric coefficients d_{33} and d_{15} of $\text{Ba}(\text{Zr}_x\text{Ti}_{1-x})\text{O}_3$ solid solutions as a function of temperature. **a** $x = 0.05$, **b** $x = 0.1$, **c** $x = 0.15$, **d** $x = 0.2$, **e** $x = 0.25$, and **f** $x = 0.3$, the experimental data of d_{33} [a,^{17,55} b,²² c, and d²⁰] denoted by squares (single crystals) and circles (ceramics)

Thermodynamic analysis

We now adopt the constructed thermodynamic potential to predict the phase structures and electromechanical properties of $\text{Ba}(\text{Zr}_x\text{Ti}_{1-x})\text{O}_3$ solid solutions, including the variations of properties in both specific compositions and continuous variations of compositions, which are also compared with some reported experimental data for verifying the reliability of the established thermodynamic potential.

Phase structures and electromechanical properties in specific compositions

We first examine phase structures and electromechanical properties of $\text{Ba}(\text{Zr}_x\text{Ti}_{1-x})\text{O}_3$ solid solutions in specific compositions, such as $\text{Ba}(\text{Zr}_x\text{Ti}_{1-x})\text{O}_3$ with composition $x = 0.05, 0.1, 0.15, 0.2, 0.25$, and 0.3 . The free energy of $\text{Ba}(\text{Zr}_x\text{Ti}_{1-x})\text{O}_3$ solid solutions under stress-free boundary condition is plotted in Supplementary Fig. S3, according to which the energy minimizing phase structures are

identified. Supplementary Fig. S3(a) indicates that $\text{Ba}(\text{Zr}_x\text{Ti}_{1-x})\text{O}_3$ with the composition $x = 0.05$ undergoes three phase transitions, and has a rhombohedral phase, an orthorhombic phase, a tetragonal phase, and a paraelectric phase in order of increasing temperature. A similar characteristic has been observed in $\text{Ba}(\text{Zr}_x\text{Ti}_{1-x})\text{O}_3$ with the composition $x = 0.1$ [Supplementary Fig. S3 (b)], while the temperature range of rhombohedral phase extends, and the temperature ranges for orthorhombic and tetragonal phases shrink. For the composition $x = 0.15$ [Supplementary Fig. S3(c)], all the phases have the same energy at T_C , suggesting a quadruple point in $\text{Ba}(\text{Zr}_x\text{Ti}_{1-x})\text{O}_3$, which has been confirmed by experimental observations.^{15,16} For the composition $x = 0.2, 0.25, 0.3$ below the Curie temperature T_C [Supplementary Figs. S3(d)–(f)], the rhombohedral phase has the lowest energy though the contrast between the three ferroelectric phases is not obvious. The phase transition temperatures can also be identified, which are marked in Supplementary Fig. S3. We compare phase transition temperatures between calculations and experiments^{13,16–22,26,50} in Supplementary Table S2, and a good agreement between them is observed, suggesting that the constructed thermodynamic potential reproduces phase transitions in $\text{Ba}(\text{Zr}_x\text{Ti}_{1-x})\text{O}_3$ solid solutions correctly.

Based on the constructed thermodynamic potential, we also calculate the electromechanical properties of $\text{Ba}(\text{Zr}_x\text{Ti}_{1-x})\text{O}_3$ solid solutions in specific compositions as a function of temperature, as shown in Figs. 1–3, in which some available experimental data from literatures are referred for comparison. Figure 1 reveals that the modulus of polarization decreases with an increase in temperature as expected, while the polarization components show discontinuous variations across phase boundaries, suggesting $\text{Ba}(\text{Zr}_x\text{Ti}_{1-x})\text{O}_3$ solid solutions having first-order phase transition. At the same temperature, the magnitude of polarization decreases with an increase in composition x . The experimental data for polarization of $\text{Ba}(\text{Zr}_x\text{Ti}_{1-x})\text{O}_3$ single-crystalline at some compositions is unavailable. For this case, we evaluate the single-crystalline polarization values P_3 by using its counterpart ceramic values P_3^c measured in experiments for comparison. The used relationships between them are $P_3 = 3P_3^c$ in tetragonal phase and $P_3 = \sqrt{2}P_3^c$ in rhombohedral phase⁶⁴ (details in the Supporting Information). The values of polarization calculated based on thermodynamic theory are consistent with those measured in experiments,^{16,20,51–54} as evidenced in Fig. 1. The dielectric and piezoelectric responses show peaks at phase transition temperatures, as seen in Figs. 2 and 3, especially a high electromechanical

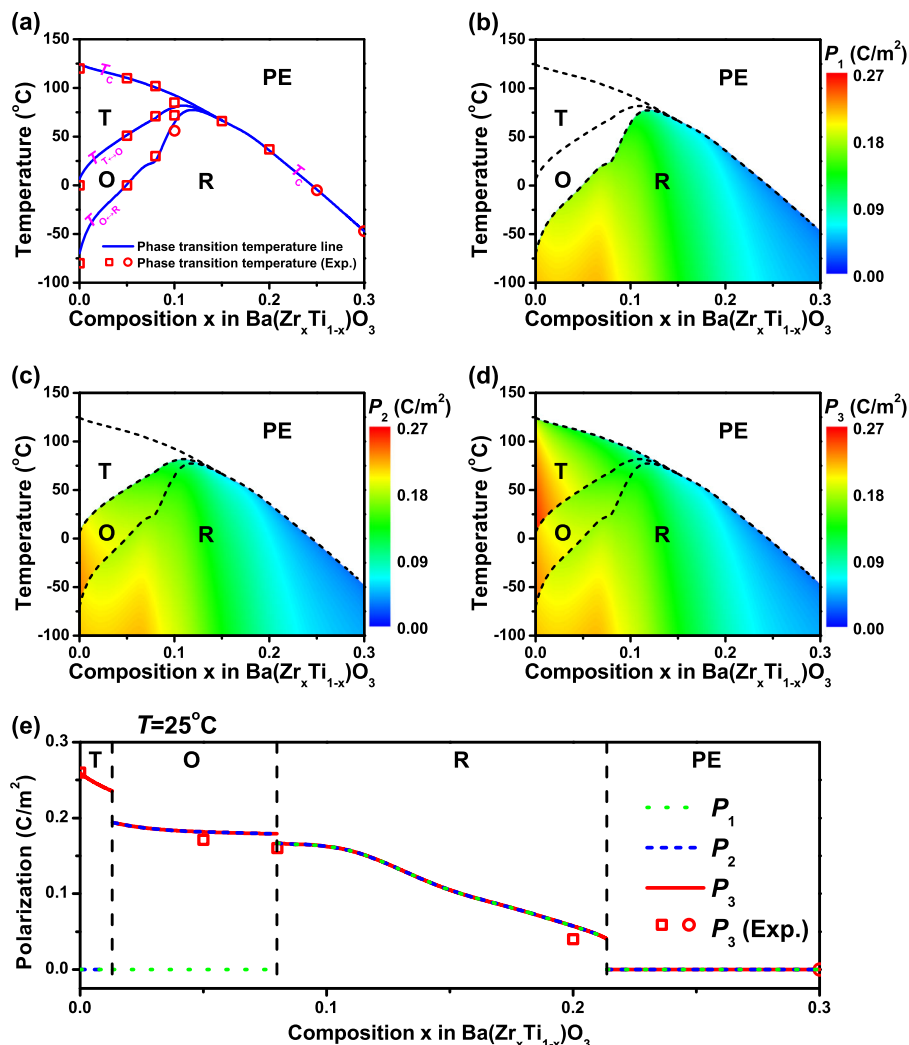


Fig. 4 **a** Temperature-composition phase diagram of $\text{Ba}(\text{Zr}_x\text{Ti}_{1-x})\text{O}_3$ solid solutions, the experimental phase transition temperatures denoted by squares (single crystals)^{13,16,18–20} and circles (ceramics).^{17,21,22} Polarization **b** P_1 , **c** P_2 , and **d** P_3 of $\text{Ba}(\text{Zr}_x\text{Ti}_{1-x})\text{O}_3$ solid solutions as a function of composition x and temperature. The phase transition temperature lines are also marked. **e** the polarization as a function of composition x at room temperature, the experimental data of P_3 denoted by squares (single-crystalline values measured in experiments)^{16,18,20,65} and circles (single-crystalline values evaluated⁶⁴ by using ceramic values measured in experiments)⁵⁴

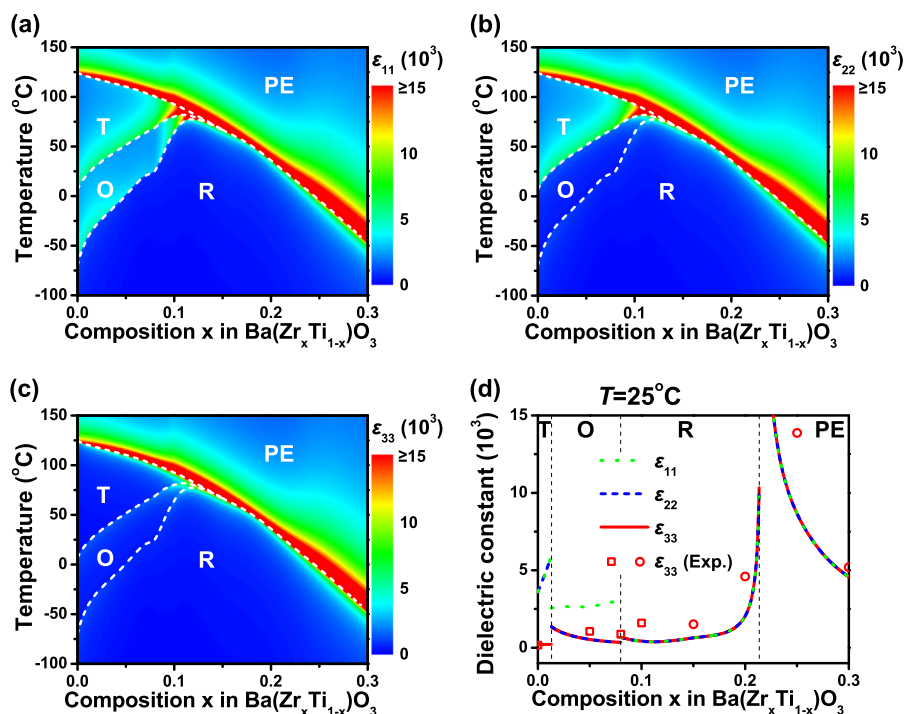


Fig. 5 Dielectric constants **a** ϵ_{11} , **b** ϵ_{22} , and **c** ϵ_{33} of $\text{Ba}(\text{Zr}_x\text{Ti}_{1-x})\text{O}_3$ solid solutions as a function of composition x and temperature. The phase transition temperature lines are also marked. **d** the dielectric constant as a function of composition x at room temperature, the experimental data of ϵ_{33} denoted by squares (single crystals)^{18,19,55,66} and circles (ceramics)^{21,56,57}

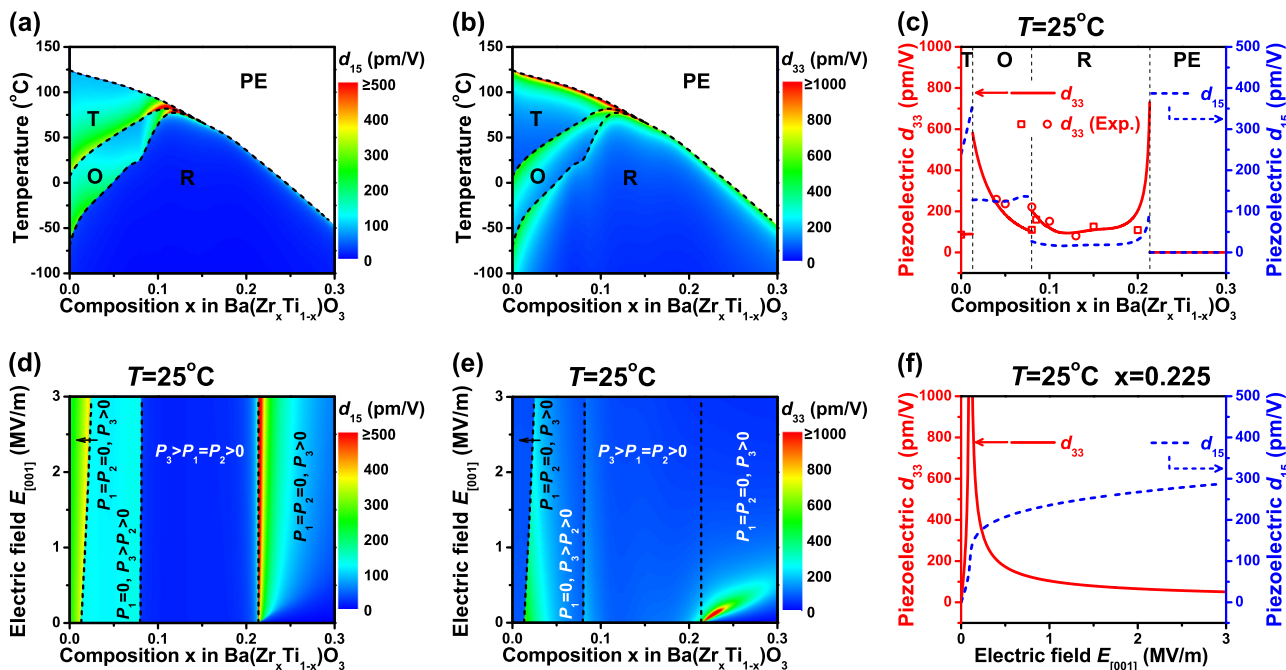


Fig. 6 Piezoelectric coefficients **a** d_{15} , and **b** d_{33} of $\text{Ba}(\text{Zr}_x\text{Ti}_{1-x})\text{O}_3$ solid solutions as a function of composition x and temperature. The phase transition temperature lines are also marked. **c** the piezoelectric coefficient as a function of composition x at room temperature, the experimental data of d_{33} denoted by squares (single crystals)^{20,55,66,67} and circles (ceramics).^{17,22} **d** d_{15} and **e** d_{33} as a function of composition x and electric field (E along $[001]$ direction) at room temperature, and **f** the corresponding piezoelectric coefficients for the case $x = 0.225$

response existing at ferroelectric–paraelectric phase transition temperature, implying that superior electromechanical properties always appear near phase boundaries. The experimental data of ϵ_{33} ^{19,21,55–57} and d_{33} ^{17,20,22,55} are also plotted in Figs. 2 and 3, showing that our thermodynamic calculation results agree with

experimental data. For some composition x , the obvious differences between the calculation values and experimental measurements can be observed, since the counterpart ceramic values are used for comparison due to the lack of experimental data for the corresponding single crystals. All the above

comparisons between thermodynamic calculations and experimental data, including the comparisons of phase structures, phase transition temperatures, and electromechanical properties, suggest that the constructed thermodynamic potential of $\text{Ba}(\text{Zr}_x\text{Ti}_{1-x})\text{O}_3$ solid solutions is reliable.

Phase diagram and electromechanical properties of continuous variations of compositions

In order to study the compositional dependence of phase structures and electromechanical properties, we fit the correlations between thermodynamic potential coefficients (Table 1) and composition x of $\text{Ba}(\text{Zr}_x\text{Ti}_{1-x})\text{O}_3$ solid solutions, as shown in Supplementary Fig. S4, the corresponding expressions of the fitting curves are listed in Supplementary Table S3. Based on these expressions of the thermodynamic potential coefficients, the temperature-composition phase diagram of $\text{Ba}(\text{Zr}_x\text{Ti}_{1-x})\text{O}_3$ solid solutions is constructed in Fig. 4a by searching for the lowest energy state between different phases. It exhibits that a paraelectric phase locates at high temperature, and a rhombohedral ferroelectric phase occupies in low temperature range, while tetragonal and orthorhombic ferroelectric phases appear only between paraelectric and rhombohedral phases at low composition x . Also, it can be found that the Curie temperature T_C decreases with an increase in composition x , while phase transition temperatures $T_{T\rightarrow O}$ and $T_{O\rightarrow R}$ show an opposite trend, and both of them increase with increasing composition x , leading to a pinched phase transition and a quadruple point near $x = 0.15$, as shown in Fig. 4a. The experimental phase transition temperatures reported in literature^{13,16–22} are marked in Fig. 4a for comparison, indicating that our calculation results are consistent with experimental results, which again confirms the reliability of thermodynamic potential constructed in this work.

The contour plot of polarization components in terms of composition and temperature is shown in Figs. 4b–d. It can be observed that $\text{Ba}(\text{Zr}_x\text{Ti}_{1-x})\text{O}_3$ solid solutions with a low composition x have high polarization, and the polarization components are discontinuous at phase boundaries, which implies first-order phase transitions in $\text{Ba}(\text{Zr}_x\text{Ti}_{1-x})\text{O}_3$ solid solutions. The contour plots of dielectric constants and piezoelectric coefficients are also presented in Figs. 5a–c and Figs. 6a–b, respectively, where the anomalies of dielectric and piezoelectric responses are observed around the phase boundaries, and superior dielectric and piezoelectric properties appear near the ferroelectric–paraelectric phase boundary, especially around quadruple point. To see this more clearly, the corresponding polarization, dielectric constants and piezoelectric coefficients at room temperature are given in Figs. 4e, 5d, and 6c. It is noticed that the tetragonal–orthorhombic (ferroelectric–ferroelectric) phase boundary is at $x = 0.013$, the orthorhombic–rhombohedral (ferroelectric–ferroelectric) phase boundary is located at $x = 0.0798$, and the rhombohedral–paraelectric (ferroelectric–paraelectric) phase boundary is at $x = 0.2135$. The dielectric and piezoelectric properties show peaks near the tetragonal–orthorhombic (ferroelectric–ferroelectric) and rhombohedral–paraelectric (ferroelectric–paraelectric) phase boundaries. Comparing the electromechanical properties among the three phase boundaries, it is evident that the ferroelectric–paraelectric phase boundary has more superior electromechanical properties, suggesting a new way to enhance electromechanical coupling in $\text{Ba}(\text{Zr}_x\text{Ti}_{1-x})\text{O}_3$ solid solutions. In addition, good agreements between calculated results and experimental data are observed in Figs. 4e, 5d, and 6c. We also examine the effect of electric field on piezoelectric coefficients at room temperature in Figs. 6d–f, where electric field induced the enhancement of piezoelectric response is obvious, especially at high composition x (for example, $x = 0.225$) near the ferroelectric–paraelectric phase boundary.

In summary, we have constructed a thermodynamic potential for $\text{Ba}(\text{Zr}_x\text{Ti}_{1-x})\text{O}_3$ solid solutions, and carried out the thermodynamic analysis of $\text{Ba}(\text{Zr}_x\text{Ti}_{1-x})\text{O}_3$ solid solutions using the constructed thermodynamic potential. It is found that the phase structures, phase transition temperatures, polarization, dielectric, and piezoelectric properties of $\text{Ba}(\text{Zr}_x\text{Ti}_{1-x})\text{O}_3$ solid solutions are reproduced well. The results also reveal that three phase boundaries, including tetragonal–orthorhombic, orthorhombic–rhombohedral, and rhombohedral–paraelectric phase boundaries, can be formed at different chemical compositions. The chemical composition-induced ferroelectric–paraelectric phase boundary has superior electromechanical properties, which suggests a new way to enhance electromechanical coupling in $\text{Ba}(\text{Zr}_x\text{Ti}_{1-x})\text{O}_3$ solid solutions. Notice that stress and strain constraints are always used to tune the phase structures and electromechanical properties in ferroelectrics.^{39,68} The constructed thermodynamic potential can be also used to predict the changes in phase structures and electromechanical properties under mechanical constraints.

METHODS

The process of determining thermodynamic potential coefficients for $\text{Ba}(\text{Zr}_x\text{Ti}_{1-x})\text{O}_3$ solid solutions is schematically illustrated in Supplementary Fig. S1. Among all thermodynamic potential coefficients, only a_1 is assumed to be dependent on temperature T , following Curie–Weiss law

$$\alpha_1 = \frac{T - T_0}{2\varepsilon_0 C} = \alpha_1^*(T - T_0), \quad (7)$$

where C , T_0 are the Curie constant and Curie–Weiss temperature, respectively. α_1 can be determined by fitting Curie temperature T_C and dielectric constants of paraelectric phase in $\text{Ba}(\text{Zr}_x\text{Ti}_{1-x})\text{O}_3$ solid solutions, as shown in Supplementary Fig. S1. The thermodynamic potential coefficients a_{11} , a_{111} , and a_{1111} need to be fitted to the phase transition temperatures T_C and $T_{T\rightarrow O}$, as well as dielectric constant and polarization of tetragonal phase. The coefficients a_{12} , a_{112} , a_{1112} , and a_{1122} are fitted to the phase transition temperatures $T_{T\rightarrow O}$ and $T_{O\rightarrow R}$, and dielectric constant and polarization of orthorhombic phase. Similarly, the coefficients a_{123} and a_{1123} can be estimated via fitting the phase transition temperature $T_{O\rightarrow R}$ and electrical properties in rhombohedral phase. After that, all the thermodynamic potential coefficients of $\text{Ba}(\text{Zr}_x\text{Ti}_{1-x})\text{O}_3$ solid solutions can be obtained, as tabulated in Table 1. It is noted that the experimental observations^{17,20,21} indicated only paraelectric and rhombohedral two phases existing in $\text{Ba}(\text{Zr}_x\text{Ti}_{1-x})\text{O}_3$ solid solutions with high concentration of Zr ($x > 0.15$). For this reason, the experimental data of paraelectric and rhombohedral phases is used to determine thermodynamic potential coefficients at high concentration x , as well as the eighth-order thermodynamic potential coefficients a_{1111} , a_{1112} , a_{1122} , and a_{1123} are set to be zero for this case.

DATA AVAILABILITY

The data that support the findings of this study are available from the corresponding author upon reasonable request.

ACKNOWLEDGEMENTS

This work was partially supported by the National Key Research and Development Program of China (2016YFA0201001), NSFC (Approval Nos. 11572276, 11772286, 11502225, 11627801, and 11402221), Project supported by Hunan Provincial Natural Science Foundation of China (2017JJ3312 and 2016JJ6146), Scientific Research Fund of Hunan Provincial Education Department (16A202 and 17B251), and Hunan Provincial Innovation Foundation for Postgraduate (CX2017B279). Lei acknowledges startup fund supported jointly by the Dean of Parks College and the Provost of the Saint Louis University.

AUTHOR CONTRIBUTIONS

Y.L. conceived the idea and designed the calculations. Y.L. and J.P. implemented constructing thermodynamic potential. Q.Y. calculated electrostrictive coefficients. All authors performed thermodynamic analysis. Y.L. and J.P. analyzed the results and wrote the paper. All authors reviewed and contributed to the final paper preparation.

ADDITIONAL INFORMATION

Supplementary information accompanies the paper on the *npj Computational Materials* website (<https://doi.org/10.1038/s41524-018-0126-3>).

Competing interests: The authors declare no competing interests.

Publisher's note: Springer Nature remains neutral with regard to jurisdictional claims in published maps and institutional affiliations.

REFERENCES

- Li, F. et al. Ultrahigh piezoelectricity in ferroelectric ceramics by design. *Nat. Mater.* **17**, 349–354 (2018).
- Hong, Z. J. et al. Stability of polar vortex lattice in ferroelectric superlattices. *Nano Lett.* **17**, 2246–2252 (2017).
- Schlom, D. G. et al. Strain tuning of ferroelectric thin films. *Annu. Rev. Mater. Res.* **37**, 589–626 (2007).
- Cao, S. G. et al. Stress-induced cubic-to-hexagonal phase transformation in perovskite nanoscale thin films. *Nano Lett.* **17**, 5148–5155 (2017).
- Velev, J. P., Burton, J. D., Zhuravlev, M. Y. & Tsybalyk, E. Y. Predictive modelling of ferroelectric tunnel junctions. *npj Comput. Mater.* **2**, 16009 (2016).
- Sharma, P. et al. Nonvolatile ferroelectric domain wall memory. *Sci. Adv.* **3**, e1700512 (2017).
- Scott, J. F. Electrocaloric materials. *Annu. Rev. Mater. Res.* **41**, 229–240 (2011).
- Wu, H. H., Zhu, J. M. & Zhang, T. Y. Pseudo-first-order phase transition for ultrahigh positive/negative electrocaloric effects in perovskite ferroelectrics. *Nano Energy* **16**, 419–427 (2015).
- Tang, Y. L. et al. Observation of a periodic array of flux-closure quadrants in strained ferroelectric PbTiO₃ films. *Science* **348**, 547–551 (2015).
- Wu, H. H. & Cohen, R. E. Electric-field-induced phase transition and electrocaloric effect in PMN-PT. *Phys. Rev. B* **96**, 054116 (2017).
- Ma, R. J. et al. Nonvolatile ferroelectric domain wall memory. *Science* **357**, 1130–1134 (2017).
- Zheng, Y., Cai, M. Q. & Woo, C. H. Critical properties of symmetric nanoscale metal-ferroelectric-metal capacitors. *Acta Mater.* **58**, 3050–3058 (2010).
- Merz, W. J. The electric and optical behavior of BaTiO₃ single-domain crystals. *Phys. Rev.* **76**, 1221–1225 (1949).
- McQuarrie, M. & Behnke, F. W. Structural and dielectric studies in the system (Ba, Ca)(Ti,Zr)O₃. *J. Am. Ceram. Soc.* **37**, 539–543 (1954).
- Maiti, T., Guo, R. Y. & Bhalla, A. S. Structure-property phase diagram of BaZr_xTi_{1-x}O₃ system. *J. Am. Ceram. Soc.* **91**, 1769–1780 (2008).
- Yu, Z., Guo, R. Y. & Bhalla, A. S. Dielectric behavior of Ba(Ti_{1-x}Zr_x)O₃ single crystals. *J. Appl. Phys.* **88**, 410–415 (2000).
- Yu, Z., Ang, C., Guo, R. Y. & Bhalla, A. S. Piezoelectric and strain properties of Ba(Ti_{1-x}Zr_x)O₃ ceramics. *J. Appl. Phys.* **92**, 1489–1493 (2002).
- Yu, Z., Guo, R. Y. & Bhalla, A. S. Dielectric polarization and strain behavior of Ba(Ti_{0.92}Zr_{0.08})O₃ single crystals. *Mater. Lett.* **57**, 349–354 (2002).
- Lee, H. Y. 6-Development of high-performance piezoelectric single crystals by using solid-state single crystal growth (SSCG) method. In Ye, Z. G. (eds) *Handbook of Advanced Dielectric, Piezoelectric and Ferroelectric Materials*, Woodhead Publishing Series in Electronic and Optical Materials, 158–172 (Woodhead Publishing, Cambridge, England, 2008).
- Yu, Z., Guo, R. Y. & Bhalla, A. S. Growth of Ba(Ti_{1-x}Zr_x)O₃ single crystal fibers by laser heated pedestal growth technique. *Ferroelectr. Lett. Sect.* **27**, 113–123 (2000).
- Yu, Z., Chen, A., Guo, R. Y. & Bhalla, A. S. Dielectric properties of Ba(Ti_{1-x}Zr_x)O₃ solid solutions. *Mater. Lett.* **61**, 326–329 (2007).
- Kalyani, A. K., Senyshyn, A. & Ranjan, R. Polymorphic phase boundaries and enhanced piezoelectric response in extended composition range in the lead free ferroelectric Ba(Ti_{1-x}Zr_x)O₃. *J. Appl. Phys.* **114**, 014102 (2013).
- Qian, X. S. et al. Giant electrocaloric response over a broad temperature range in modified BaTiO₃ ceramics. *Adv. Funct. Mater.* **24**, 1300–1305 (2014).
- Devonshire, A. F. XCVI. Theory of barium titanate Part I. *Philos. Mag.* **40**, 1040–1063 (1949).
- Marton, P., Rychetsky, I. & Hlinka, J. Domain walls of ferroelectric BaTiO₃ within the Ginzburg-Landau-Devonshire phenomenological model. *Phys. Rev. B* **81**, 144125 (2010).
- Li, Y. L., Cross, L. E. & Chen, L. Q. A phenomenological thermodynamic potential for BaTiO₃ single crystals. *J. Appl. Phys.* **98**, 064101 (2005).
- Khakpash, N., Khassaf, H., Rossetti, G. A. Jr. & Alpay, S. P. Misfit strain phase diagrams of epitaxial PMN-PT films. *Appl. Phys. Lett.* **106**, 082905 (2015).
- Wang, J. & Zhang, T. Y. Effects of nonequally biaxial misfit strains on the phase diagram and dielectric properties of epitaxial ferroelectric thin films. *Appl. Phys. Lett.* **86**, 192905 (2005).
- Pertsev, N. A., Zembilgotov, A. G. & Tagantsev, A. K. Effect of mechanical boundary conditions on phase diagrams of epitaxial ferroelectric thin films. *Phys. Rev. Lett.* **80**, 1988–1991 (1998).
- Pertsev, N. A. & Kohlstedt, H. Elastic stabilization of a single-domain ferroelectric state in nanoscale capacitors and tunnel junctions. *Phys. Rev. Lett.* **98**, 257603 (2007).
- Lv, P., Wang, L. H. & Lynch, C. S. A phenomenological thermodynamic energy function for PIN-PMN-PT relaxor ferroelectric single crystals. *Acta Mater.* **137**, 93–102 (2017).
- Qiu, Y. et al. Giant electrocaloric effect in ferroelectric ultrathin films at room temperature mediated by flexoelectric effect and work function. *J. Appl. Phys.* **122**, 024103 (2017).
- Mangeri, J., Pitike, K. C., Alpay, S. P. & Nakhmanson, S. Amplitudon and phason modes of electrocaloric energy interconversion. *npj Comput. Mater.* **2**, 16020 (2016).
- Liu, Y. Y. et al. Controlling magnetoelectric coupling by nanoscale phase transformation in strain engineered bismuth ferrite. *Nanoscale* **4**, 3175–3183 (2012).
- Karpinsky, D. V. et al. Thermodynamic potential and phase diagram for multi-ferroic bismuth ferrite (BiFeO₃). *npj Comput. Mater.* **3**, 20 (2017).
- Haun, M. J., Zhuang, Z. Q., Furman, E., Jang, S. J. & Cross, L. E. Thermodynamic theory of the lead zirconatetitanate solid solution system, part III: Curie constant and sixth-order polarization interaction dielectric stiffness coefficients. *Ferroelectrics* **99**, 45–54 (1989).
- Bell, A. J. & Cross, L. E. A phenomenological gibbs function for BaTiO₃ giving correct e field dependence of all ferroelectric phase changes. *Ferroelectrics* **59**, 197–203 (1984).
- Wang, Y. L. et al. Landau thermodynamic potential for BaTiO₃. *J. Appl. Phys.* **101**, 104115 (2007).
- Wang, J. J., Wu, P. P., Ma, X. Q. & Chen, L. Q. Temperature-pressure phase diagram and ferroelectric properties of BaTiO₃ single crystal based on a modified Landau potential. *J. Appl. Phys.* **108**, 114105 (2010).
- Salahuddin, S. & Datta, S. Use of negative capacitance to provide voltage amplification for low power nanoscale devices. *Nano Lett.* **8**, 405–410 (2008).
- Karthik, J. & Martin, L. W. Pyroelectric properties of polydomain epitaxial Pb(Zr_{1-x}Ti_x)O₃ thin films. *Phys. Rev. B* **84**, 024102 (2011).
- Liu, Y. Y. & Li, J. Y. Shear-driven morphotropic phase boundary in epitaxial ferroelectric thin films. *Phys. Rev. B* **84**, 132104 (2011).
- Li, Y. L. & Chen, L. Q. Temperature-strain phase diagram for BaTiO₃ thin films. *Appl. Phys. Lett.* **88**, 072905 (2006).
- Chen, L. Q. Phase-field method of phase transitions/domain structures in ferroelectric thin films: A review. *J. Am. Ceram. Soc.* **91**, 1835–1844 (2008).
- Wang, J., Li, Y. L., Chen, L. Q. & Zhang, T. Y. The effect of mechanical strains on the ferroelectric and dielectric properties of a model single crystal - phase field simulation. *Acta Mater.* **53**, 2495–2507 (2005).
- Su, Y., Liu, N. & Weng, G. J. A phase field study of frequency dependence and grain-size effects in nanocrystalline ferroelectric polycrystals. *Acta Mater.* **87**, 293–308 (2015).
- Haun, M. J., Furman, E., Jang, S. J., McKinstry, H. A. & Cross, L. E. Thermodynamic theory of PbTiO₃. *J. Appl. Phys.* **62**, 3331–3338 (1987).
- Liu, Y. Y., Zhu, Z. X., Li, J. F. & Li, J. Y. Misfit strain modulated phase structures of epitaxial Pb(Zr_{1-x}Ti_x)O₃ thin films: The effect of substrate and film thickness. *Mech. Mater.* **42**, 816–826 (2010).
- Liu, Y. Y., Yang, L. & Li, J. Y. Strain-engineered orthorhombic-rhombohedral phase boundary in epitaxial bismuth ferrite films. *J. Appl. Phys.* **113**, 183524 (2013).
- Peng, J. L. et al. Phenomenological thermodynamic potentials for bulk and thin-film Ba(Zr_{0.08}Ti_{0.92})O₃ single crystals. *J. Appl. Phys.* **119**, 204103 (2016).
- Tian, Y., Chao, X. L., Wei, L. L., Liang, P. F. & Yang, Z. P. Phase transition behavior and electrical properties of lead-free (Ba_{1-x}Ca_x)(Zr_{0.1}Ti_{0.9})O₃ piezoelectric ceramics. *J. Appl. Phys.* **113**, 184107 (2013).
- Mahesh, M. L. V., Prasad, V. V. B. & James, A. R. Enhanced dielectric and ferroelectric properties of lead-free Ba(Zr_{0.15}Ti_{0.85})O₃ ceramics compacted by cold isostatic pressing. *J. Alloy. Compd.* **611**, 43–49 (2014).
- Kruea-In, C., Eitssayeam, S., Pengpat, K., Rujjanagul, G. & Tunkasiri, T. Effects of vibro-milling on relaxor ferroelectric behavior and phase transition of lead-free Ba(Zr_{0.25}Ti_{0.75})O₃ ceramics. *Phase Transit.* **83**, 942–949 (2010).
- Yu, Z., Ang, C., Guo, R. Y. & Bhalla, A. S. Ferroelectric-relaxor behavior of Ba(Ti_{0.7}Zr_{0.3})O₃ ceramics. *J. Appl. Phys.* **92**, 2655–2657 (2002).
- Yu, Z., Guo, R. Y. & Bhalla, A. S. Orientation dependence of the ferroelectric and piezoelectric behavior of Ba(Ti_{1-x}Zr_x)O₃ single crystals. *Appl. Phys. Lett.* **77**, 1535–1537 (2000).
- Bao, H. X., Zhou, C., Xue, D. Z., Gao, J. H. & Ren, X. B. A modified lead-free piezoelectric BZT-xBCT system with higher T_C. *J. Phys. D: Appl. Phys.* **43**, 465401 (2010).
- Fu, C. L., Pan, F. S., Cai, W., Deng, X. L. & Liu, X. W. Microstructures and dielectric properties of BaZr_{0.2}Ti_{0.8}O₃ ceramics. *J. Phys.: Conf. Ser.* **152**, 012075 (2009).

58. Pohlmann, H., Wang, J. J., Wang, B. & Chen, L. Q. A thermodynamic potential and the temperature-composition phase diagram for single-crystalline $K_{1-x}Na_xNbO_3$ ($0 \leq x \leq 0.5$). *Appl. Phys. Lett.* **110**, 102906 (2017).
59. Huang, Y. H. et al. A thermodynamic potential, energy storage performances, and electrocaloric effects of $Ba_{1-x}Sr_xTiO_3$ single crystals. *Appl. Phys. Lett.* **112**, 102901 (2018).
60. Shakhovoy, R. A., Shirokov, V. B. & Yuzyuk, Y. I. Phase diagrams of $BaTiO_3/BaZrO_3$ superlattices. *Ferroelectrics* **444**, 168–176 (2013).
61. Yamada, T. Electromechanical properties of oxygen-octahedra ferroelectric crystals. *J. Appl. Phys.* **43**, 328–338 (1972).
62. Wang, J. J., Meng, F. Y., Ma, X. Q., Xu, M. X. & Chen, L. Q. Lattice, elastic, polarization, and electrostrictive properties of $BaTiO_3$ from first-principles. *J. Appl. Phys.* **108**, 034107 (2010).
63. Hayward, S. A. & Salje, E. K. H. The pressure-temperature phase diagram of $BaTiO_3$: a macroscopic description of the low-temperature behaviour. *J. Phys.: Condens. Matter* **14**, L599–L604 (2002).
64. Li, J. Y., Rogan, R. C., Üstündag, E. & Bhattacharya, K. Domain switching in polycrystalline ferroelectric ceramics. *Nat. Mater.* **4**, 776–781 (2005).
65. Wieder, H. H. Electrical behavior of barium titanate single crystals at low temperatures. *Phys. Rev.* **99**, 1161–1165 (1955).
66. Berlincourt, D. & Jaffe, H. Elastic and piezoelectric coefficients of single-crystal barium titanate. *Phys. Rev.* **111**, 143–148 (1958).
67. Rehrig, P. W. et al. Piezoelectric properties of zirconium-doped barium titanate single crystals grown by templated grain growth. *J. Appl. Phys.* **86**, 1657–1661 (1999).
68. Zhou, M. J., Wang, J. J., Chen, L. Q. & Nan, C. W. Strain, temperature, and electric-field effects on the phase transition and piezoelectric responses of $K_{0.5}Na_{0.5}NbO_3$ thin films. *J. Appl. Phys.* **123**, 154106 (2018).



Open Access This article is licensed under a Creative Commons Attribution 4.0 International License, which permits use, sharing, adaptation, distribution and reproduction in any medium or format, as long as you give appropriate credit to the original author(s) and the source, provide a link to the Creative Commons license, and indicate if changes were made. The images or other third party material in this article are included in the article's Creative Commons license, unless indicated otherwise in a credit line to the material. If material is not included in the article's Creative Commons license and your intended use is not permitted by statutory regulation or exceeds the permitted use, you will need to obtain permission directly from the copyright holder. To view a copy of this license, visit <http://creativecommons.org/licenses/by/4.0/>.

© The Author(s) 2018